Numerical Investigation of Atmospheric Boundary Layer Control in Wind Farms with Multirotor Systems

Martins, Flavio A.C.; Ferreira, Carlos S.; Van Zuijlen, Alexander

DOI
10.1088/1742-6596/2767/7/072006

Publication date
2024

Document Version
Final published version

Published in
Journal of Physics: Conference Series

Citation (APA)
Martins, F. A. C., Ferreira, C. S., & Van Zuijlen, A. (2024). Numerical Investigation of Atmospheric Boundary Layer Control in Wind Farms with Multirotor Systems. *Journal of Physics: Conference Series*, *2767*(7), Article 072006. https://doi.org/10.1088/1742-6596/2767/7/072006

Numerical Investigation of Atmospheric Boundary Layer Control in Wind Farms with Multirotor Systems

Journal of Physics: Conference Series **2767** (2024) 072006 doi:10.1088/1742-6596/2767/7/072006

Numerical Investigation of Atmospheric Boundary Layer Control in Wind Farms with Multirotor Systems

Flavio A. C. Martins, Carlos S. Ferreira, Alexander van Zuijlen

Faculty of Aerospace Engineering, Flow Physics and Technology Department, Wind Energy Section. Delft University of Technology, Kluyverweg 1, Delft, The Netherlands

E-mail: f.m.martins@tudelft.nl

Abstract. This study investigates the near-wake aerodynamics of actuator disks (multirotor devices) paired with lift-generating devices (rotor-sized wings, dubbed ABL-control devices). These rotor-sized wings generate vortical structures that enhance the vertical momentum flux from above the atmospheric boundary layer (ABL) into the wind farm, aiding wake recovery. Using three-dimensional actuator surface models based on Momentum theory, the study employs steady-state Reynolds-averaged Navier–Stokes computations in `OpenFOAM` to address the current proof-of-concept model. The numerical results of this paper are validated with a comparison against the experimental results of a scaled multirotor device in a wind tunnel. The performance of the ABL-controlling devices is evaluated through the wind farm's total pressure and vertical momentum flux. Results indicate that ABL-control significantly accelerates wake recovery, with designs featuring two or four ABL-control devices achieving 95% total pressure recovery at $x/D \approx 5$, one order of magnitude shorter than the baseline setup without ABL-control.

1. Introduction

With the recognition that wind energy may play a significant role in the decarbonization of the atmosphere, the transition to wind energy is expected to grow, with both on- and off-shore wind farms foreseen to cover increasingly larger surface areas. Notably, the implementation of extensive wind farming capable of meeting international targets for wind power expansion faces challenges in technical, environmental, economic, and social acceptance aspects related to current large-scale wind farming technologies. When considering large-scale wind farm layouts, the total drag induced by all turbines in the farm can alter the equilibrium in the atmospheric boundary layer. Specifically, with a characteristic height of the atmospheric boundary layer (ABL) at about one km, wind farms with a surface land area exceeding 10–20 km^2 can approach the asymptotic limit of an "infinite" wind farm, where the boundary layer flow may approach a fully developed regime, and most kinetic energy entrainment occurs above the farm [1]. Since velocity fluctuations are typically the only source of kinetic energy, lower fluxes of vertical flow across the ABL in an infinite wind farm can limit the power production of the wind turbines.

Blade aerodynamics and single turbine optimization for maximum power extraction are widely explored topics, commonly based on blade-element-momentum theory for rotor aerodynamics [2]. Many studies also focus on improving the power output of wind farms via wake-deflection strategies. In horizontal-axis wind turbines, wake-deflection is often achieved by

intentionally yawing the rotor out of the wind [3]; whereas in vertical-axis wind turbine farms, wake-deflection is usually achieved via modifications in the rotor blades layout that induce the generation of momentum-carrying vorticity in the wake [4]. In contrast, studies on ABL-control strategies for large wind farms are far less prevalent. The current work describes and assesses multirotor setups consisting of paired multirotors and rotor-sized wings, dubbed ABL-control devices, in the near-wake region (see panel (b) in Fig.1). In this novel setup, the rotor-sized wings create vortical structures that can accelerate the vertical momentum flux from the wind farm flow to the flow above the ABL, augmenting the wind farm's net power production.

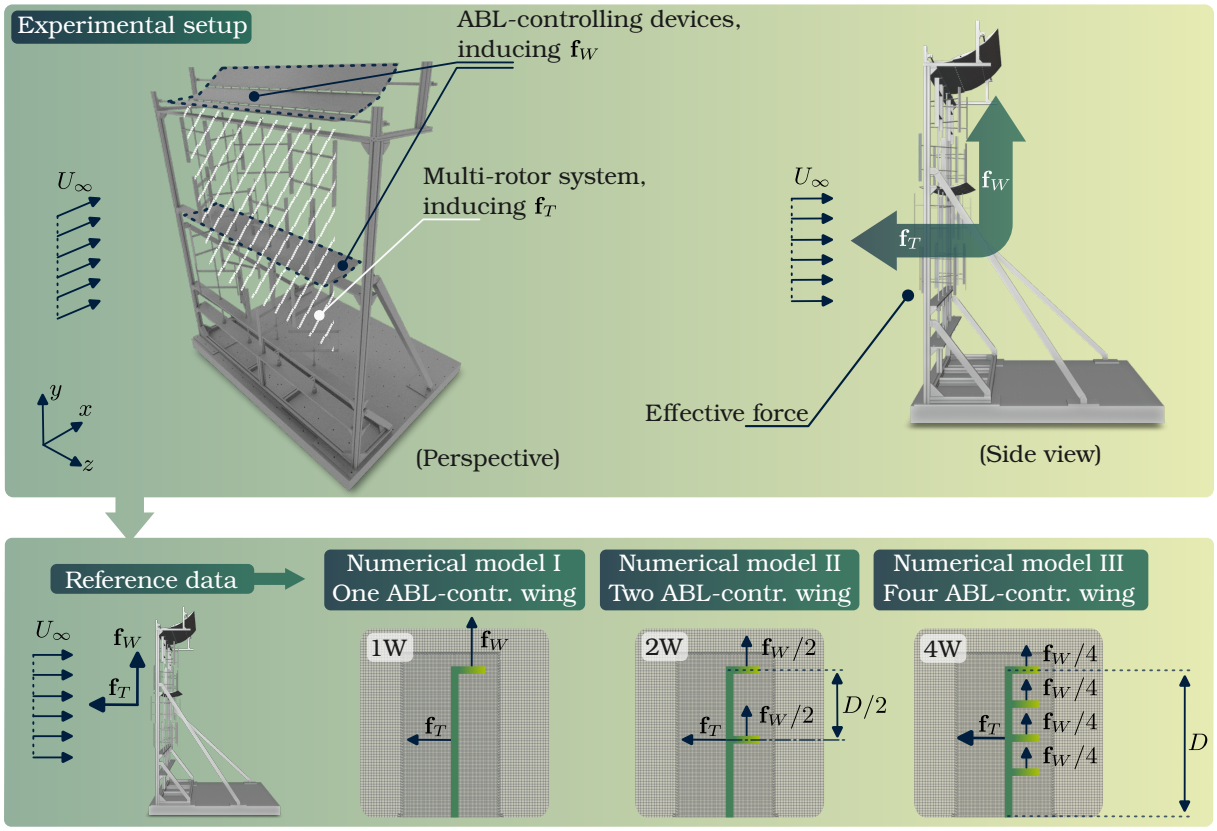

Figure 1. The figure provides a detailed view of the experimental setup providing the reference data for the numerical models. In this work, three numerical models of ABL-controlled flows, namely 1W, 2W and 4W, are assessed.

In this work, multirotor and ABL-controlling devices are parameterized with three-dimensional actuator surface models based on Momentum theory. Steady-state Reynolds-averaged Navier-Stokes (RANS) computations, performed in `OpenFOAM`, are proposed to address the current proof-of-concept work. The performance of the ABL-controlling devices is quantified via the wind farm's total pressure. The vertical momentum flux through the ABL is also investigated. Experimental observations of a scaled multirotor system set up in TU Delft's open-jet facility accompany the numerical results from this study.

This paper is organized as follows. In § 2, we present the numerical setup and the description of the assessed test cases. In § 3, we present the grid-independence analysis results and the numerical model's validation against a scaled experimental dataset. In § 3.2, we discuss the main flow features of the ABL-controlled flows via analyses of the velocity and vorticity fields for different possible ABL device configurations. In § 3.3, we quantify the performance of the

different designs by analyzing the vertical momentum flux and wake total pressure.

2. Methodology

We model the flow within the wind farm using the steady-state, incompressible Reynolds-Averaged Navier-Stokes (RANS) equations:

$$\nabla \cdot \overline{\mathbf{u}} = 0 \tag{1}$$

$$(\overline{\mathbf{u}} \cdot \nabla)\,\overline{\mathbf{u}} = -\frac{1}{\rho}\nabla \overline{p} + \nabla \cdot (\nu \nabla \overline{\mathbf{u}}) - \nabla \cdot \mathbf{R} + \frac{1}{\rho}\mathbf{f}_T + \frac{1}{\rho}\mathbf{f}_W, \tag{2}$$

where $\mathbf{u} = u_x\hat{\imath} + u_y\hat{\imath} + u_z\hat{k}$ is the velocity, p is the pressure, ν, is the kinematic viscosity and $\mathbf{f}_T$ and $\mathbf{f}_W$ are the body forcing terms associated with the multirotor systems and ABL-controlling devices, respectively. The overbar represents the mean component of the respective variable. The turbulent flow is modeled using the shear-stress-transport (SST) $k-\omega$ model [5], based on an uncertainty assessment conducted by Hornshøj-Møller et al. (2021) [6]. The eddy viscosity is computed from the turbulent kinetic energy k and the specific dissipation rate ω, which are estimated using $k = 3/2(T_{u,\infty}U_\infty)^2$ and $\omega = k^{1/2}/C_\mu^{1/4}D$, respectively. Here, $T_{u,\infty}$ and U_∞ denote, respectively, the turbulence intensity and reference velocity in the unperturbed, far-field flow, such that $U_\infty := |\overline{\mathbf{u}}_\infty|$; $C\mu$ is a constant equal to 0.09, and D is the side length of the multirotor, adopted here as the reference length scale. The effects of the multirotor systems on the flow are modeled as a body force $\mathbf{f}_T$, such that the net rotor-induced force is uniformly distributed across the finite-volume cells comprising the rotor's breadth. The total rotor forces, $\mathbf{f}_T$, act as a source in the momentum equation in Eq. 2, and it is determined using:

$$\mathbf{f}_T = -\frac{1}{2}\left(\rho D^2 U_\infty^2\right) C_T\, \hat{\imath}, \tag{3}$$

where U_∞ in the reference velocity in the unperturbed, far-field flow, ρ is the air density, and C_T is the rotor's effective thrust coefficient measured in an open jet facility. The ABL-controlling devices are likewise modeled as source terms in the momentum equation using:

$$\mathbf{f}_W = \frac{1}{2}\left(\rho D^2 U_\infty^2\right) C_W\, \hat{\imath}, \tag{4}$$

where C_W is the experimentally-measured effective lift-force coefficient. The numerical setup is illustrated in panel (b) of Fig.1. The force coefficients C_T and C_W are determined from experimental observations of a single physical twin-rotor multirotor system with ABL-controlling wings at TU Delft's Open Jet Facility. Note that due to constant, homogeneously distributed aerodynamic loadings, the current models are relatively steady, and thus, an unsteady model is deemed peripheral. Moreover, since the primary mechanism for energy transportation relies on the generation and advection of large-scale wing-tip vortical structures, higher-fidelity models (e.g., Large-Eddy simulations) that can better resolve the smaller scale vortex dynamics are deemed unnecessary for this investigation. As will be further discussed in § 3, the current steady RANS model is sufficient for the analysis conducted.

2.1. Numerical setup

In this work, all numerical computations are performed using `OpenFOAM` v8 [7], along with the momentum sources, i.e., $\mathbf{f}_T$ and $\mathbf{f}_W$, computed using a cell-weighted-distributed momentum source code written by the authors. The momentum sources are distributed in a cell-volume-weighted fashion onto the cell centers comprising the respective multirotor and ABL-controlling

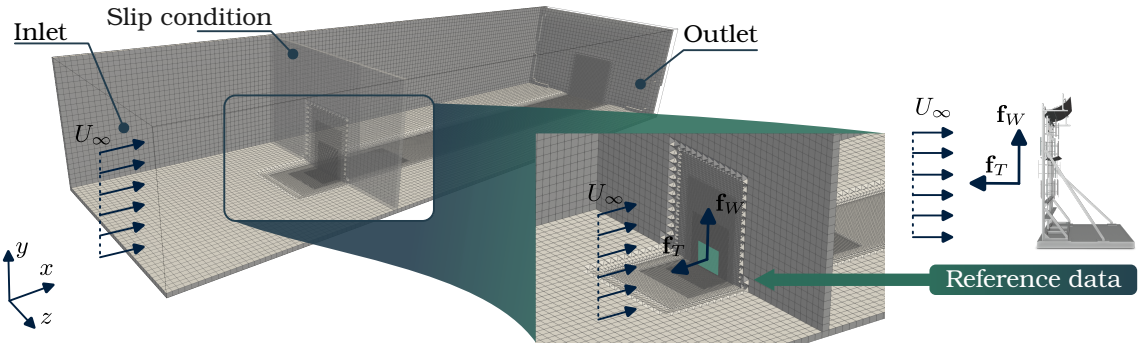

Figure 2. The figure depicts the computational grid and boundary conditions.

systems. A steady-state, incompressible solver (i.e., `simpleFoam`) is selected for the simulations, employing the SIMPLE method for pressure-velocity coupling.

Gaussian integration was used with different interpolation schemes for the spatial discretization of differential operators. The second-order linear interpolation was employed for gradient terms, the second-order bounded upwind interpolation for divergence terms, and the second-order linear corrected interpolation scheme was used for Laplacian terms. The Geometric Agglomerated Algebraic Multigrid (V-cycle) solver was adopted with the Gauss-Seidel preconditioner method for pressure and its symmetrical version for velocity and turbulence variables. An error tolerance of 1×10^{-8} was adopted for all smooth solvers. The relaxation parameters were set to 0.3 for pressure and 0.7 for velocity and turbulence variables (i.e., k and ω), as is conventional in the literature [8].

Neutral ABL modeling involves inlet boundary conditions providing log-law-type ground-normal inflow boundary conditions for wind velocity and turbulence quantities [9]. However, for this proof-of-concept work, it is deemed more convenient to model the inlet boundary condition with a uniform (Dirichlet) profile for velocity and turbulence-model quantities and a zero-gradient (Neumann) boundary condition for pressure. This simplification assumption allows for the generalization of the current results by eliminating uncertainties associated with introducing ground-normal velocity gradients in the model. The sides of the domain are modeled as slip (Neumann) boundary conditions. The outlet is modeled as a free-stream flow condition and a zero-pressure boundary condition for pressure. The free-stream wind velocity, U_∞, renders a multirotor-size-based Reynolds number of $Re := DU_\infty \nu^{-1}$, approximately $Re_D \approx 2.7 \times 10^5$.

The computational domain extends $50D \times 20D \times 10D$ in the downwind (x), spanwise (z), and vertical (y) directions, respectively. The multirotor array is located $10D$ downwind of the inlet. These domain dimensions satisfy all minimum domain-sizing requirements to minimize the boundary effects on the performance of the turbine [10]. The multirotor system extends a cross-sectional area of $1D \times 1D$ ($\hat{\imath} \times \hat{k}$) and a width of two finite-volume cells in the downwind direction, $\hat{\imath}$. The ABL-controlling wings are $1D$-long in the spanwise direction and two finite-volume cells wide in the streamwise and vertical directions. The authors adopted the two-cell breath to guarantee the stability of the finite-volume solver.

3. Results

Four setups are investigated in this study, comprising a multirotor system with four, two, one, or no ABL-controlling devices. The free-stream turbulent flow is modeled with a low turbulence intensity of $T_{u,\infty} = 1\%$, approximating the turbulence intensity levels of the reference open-jet facility data in order of magnitude. The thrust coefficient for the numerical model is based on experimental observations for a scaled multirotor system at a tip-speed ratio of 3.1, resulting

in approximately $C_T = 0.71$. The total lift force coefficient of the wing is about $C_W = 0.82$. The total lift force is homogeneously distributed among all the wings in a cell-weighted fashion, ensuring that C_W remains constant across all cases.

3.1. Grid-independence analysis and model validation

A Cartesian-type tetrahedral mesh with finer cell sizing near the multirotor system is adopted to capture high gradients in the flow. The computational domain is also finely seeded along the wake to capture vorticity along the wake's stream tube surface. The sizing of the cell elements was set to minimize the grid-sizing influence on the total pressure, $p_t := p + 1/2|\overline{\mathbf{u}}|^2\rho$. Results are considered grid-independent when the total pressure sampled at different planes downwind of the turbines is insensitive (i.e., less than a 0.05% difference) to further grid refinements. Grid refinements were performed by approximately halving the diameter of the cell elements, Δl, between two consecutive grid refinements. From the grid-independence analysis, it was found that a grid with cell sizings of $\Delta l/D \approx 0.03$ in the near-wake region (a $4D \times 2D \times 2D$-wide box centered on the multirotor device), $\Delta l/D \approx 0.09$ along the wake, and $\Delta l/D \approx 0.27$ in the far-field was sufficient for grid-independent results. The results presented in the following sections were computed using the 'Fine' mesh, which is shown in Fig. 1.

Table 1. Results of the grid-independence analysis. The "Fine" mesh is adopted in this study.

Mesh	Size of smallest grid element $\Delta l/D$	Number of finite-volume cells	Relative error in total wake pressure, p_t
Coarse	0.07	1.9×10^5	-
Medium	0.05	5.4×10^5	0.06%
Fine	0.03	2.4×10^6	0.03%
Dense	0.02	7.6×10^6	0.03%

The test case in Fig. 3 consists of a setup with an actuator wing at the top of the multirotor device ($y/D = 1.1$) and a second actuator wing at the center of the device (i.e., $y/D = 0.6$). The figure also displays the u_x fields at $x/D = 1$. The figure highlights the strong correlation between the reference experimental data and the current steady numerical model, evident from the induction field behind the multirotor system and the size and shape of the two wing-tip vortices at $y/D \approx 1.25$.

3.2. Wake characteristics

Figure 4 depicts the wake behind the multirotor system, represented by downwind-velocity colored fields, u_x/U_∞, at various downstream planes. White lines outline the silhouette of the multirotor system in all panels. The top row illustrates the wake of the reference case (Baseline), a conventional flow without ABL-controlling devices. Subsequent rows showcase results for increasing numbers of ABL-controlling devices ('1W': one wing, '2W': two wings, $\cdots$). A prevalent vertical motion with crossflow expansion characterizes the ABL-controlled wakes until the outer shear layers become unstable and break down under viscous diffusion. The figure also captures the rapid ascent of wakes in cases 1W, 2W, and 4W, facilitated by strong counter-rotating wing-tip vortices. Notably, without ABL-controlling devices (i.e., the Baseline case), wake re-energizing relies solely on turbulent mixing.

For the case 1W, fluid parcels near the middle plane $z/D = 0$ ascend more quickly than those near the two wing-tip vortices at $z/D \approx \pm 0.5$, which are advected to the flow above the turbine at lower vertical speeds. In the 2W and 4W cases (third and fourth rows of Fig. 4), the efficient upward advection of high-induction fluid parcels behind the multirotor system is notably improved compared to the case 1W. This enhanced efficiency is evident in the the

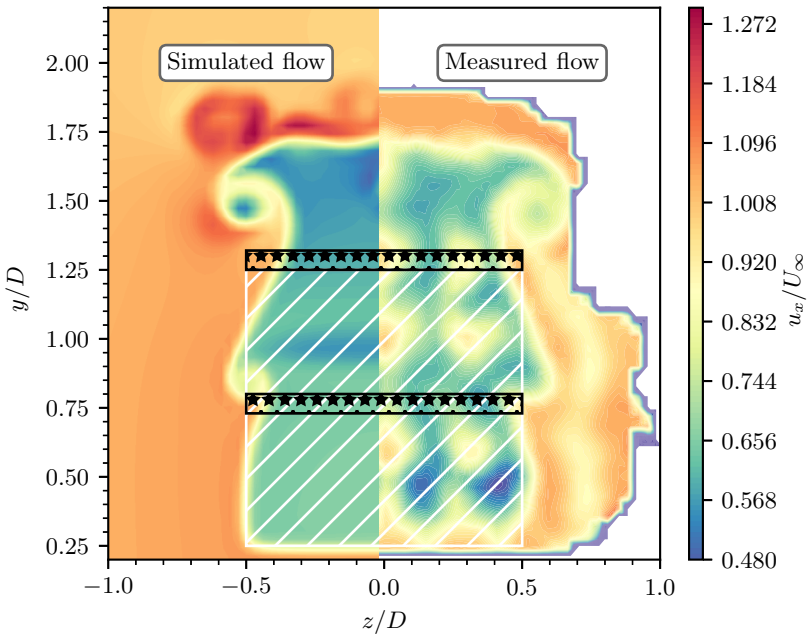

Figure 3. Comparison between simulated (left) and experimental (right) u_x-velocity colored fields at $x/D = 1$ behind the ABL-controlled setups. The setup consists of a multirotor system (represented by the hashed region) with 2 wings (highlighted as $\star$-symbols). The setup induces $C_T \approx 0.72$ and $C_W \approx 0.88$.

velocity-deficit region behind the rotor, which is substantially narrower in cases 2W and 4W compared to 1W. However, Despite the more efficient upwards advection of the wake promoted by the extra wings of cases 2W and 4W, the velocity-deficit flow is, on average, lower in the ABL in these cases compared to the results for case 1W. For instance, at the downstream plane $x/D = 7$, the maximum height of the wake is $y/D \approx 2.4$ for the 1W case, whereas for the 2- and 4W cases, the maximum height of the wake is $y/D \approx 2.1$. It is important to note that the total vertical force is the same in all cases

To comprehend the flow mechanisms driving the upward motion of the wake and, more specifically, why velocity-deficit fluid parcels are advected at different rates depending on their location across the wake, analyses of the velocity field are insufficient. It is deemed essential to evaluate the flow through the vorticity fields. Figure 5 illustrates downwind-vorticity colored, $\omega_x D/U_\infty$, cross-sectional planes of the flow for an increasing number of ABL-controlling wings. In the case 1W, the downwind-vorticity-colored fields reveal the two counter-rotating wing-tip vortices formed behind the multirotor system. These vortices cause the upward motion of the wake along the middle plane $z/D = 0$, while inducing downwash motion in the high-momentum flow above the multirotor system for $z/D < -0.5$ and $z/D > 0.5$.

In the cases 2W and 4W, the average upward motion of the wake is also observed. However, the behavior of the flow parcels near the planes $z/D \approx \pm 0.5$ is considerably different from that observed in the same planes for the case 1W. Specifically, in the cases 2W and 4W, the multiple generated wing-tip vortices coalesce into two counter-rotating vortices at $y/D \approx 2$ as $z/D \to \infty$. Although these two merged vortices also counter-rotate and induce a similar ascent motion to the wake near the symmetry plane $z/D = 0$ to that observed for the case 1W, it is evident that during the vortex coalescence process, the individual wing-tip vortices also induce the crossflow stretching of the resulting large vortical structures (see the $x/D = 2$ panels of cases 2W and 4W). Moreover, before the coalescing process is completed, the different induction fields of the

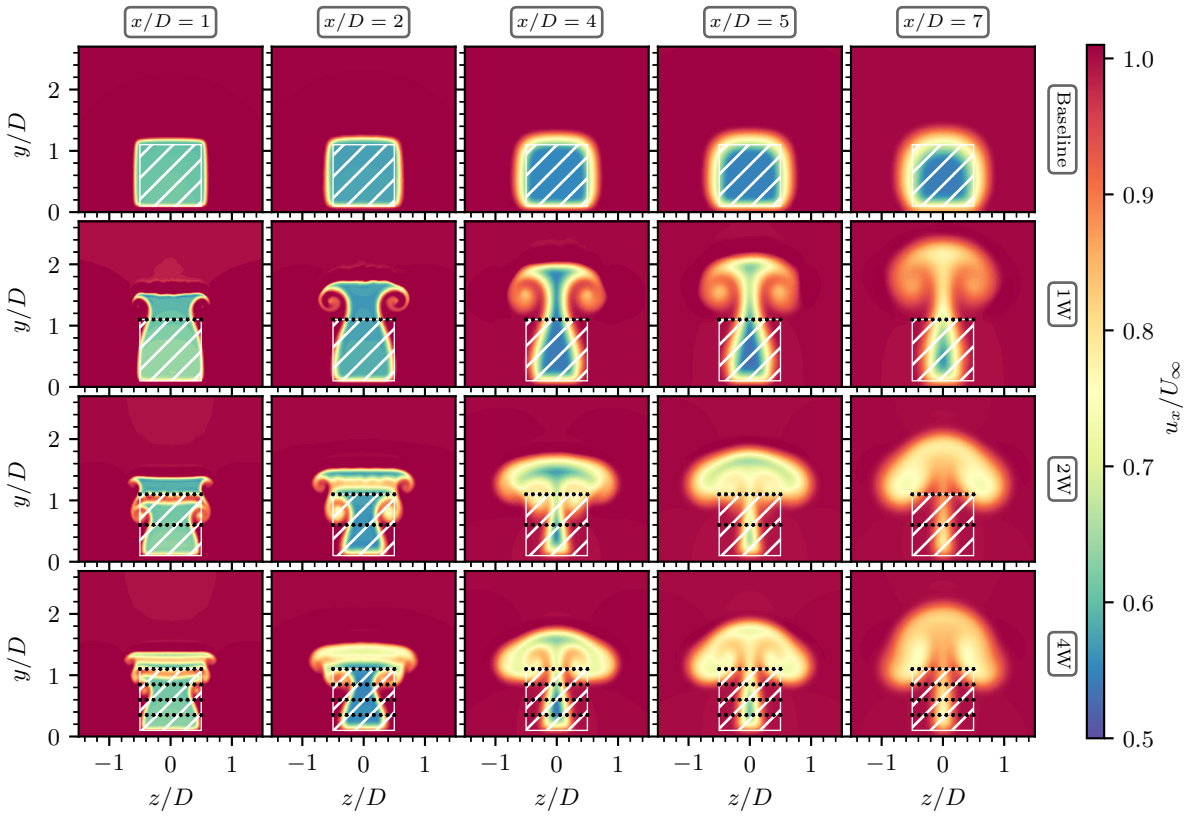

Figure 4. Downwind velocity contours reveal a rotor's wake with and without ABL-controlling devices. The rotor's projected area is represented as a hashed region. The top-to-bottom rows show results for 0, 1, 2, and 4 ABL-controlling wings (represented as $\star$ symbols), respectively.

individual wing-tip vortices slow down the average upward advection speed of the resulting large vortical structures.

Given that the wing-tip vortices are the primary mechanism for lifting the low-momentum wake flow upwards while moving the high-momentum ABL flow downwards, a simplified analysis of the flow in view of the Kutta-Joukowski theorem is deemed relevant. Let us denote the circulation around a closed contour in the crossflow plane by Γ_x. If we adopt the conservative flow assumption, the Kutta-Joukowski theorem expresses that the circulation associated with the wing-tip vortices of the case 1W can be approximated by $\Gamma_x = -C_W U_\infty D/2$. Moreover, it is also known from potential flow theory that the tangential velocity u_θ induced by a point-vortex idealization at a distance r from the same point-vortex is $u_\theta = -\Gamma_x/2\pi r$. Thus, if we approximate the current flows to a conservative flow idealization, it is straightforward that the vertical velocity $u_y(z = 0)$ induced at the symmetry plane $z/D = 0$ of the flow due to the two wing-tip vortices for a single ABL-controlling wing is $u_y(z = 0) \sim 2u_\theta \sim C_W U_\infty/\pi\hat{\imath}$. This result shows that, due to the action of the wing-tip vortices, fast upward advection of fluid parcels is expected near the $z/D = 0$ plane. On the other hand, the vertical velocity induced on one vortex by another is approximately $u_y(z/D = \pm - 0.5) \sim C_W U_\infty/4\pi\hat{\imath}$, i.e., $u_y(z/D = \pm - 0.5)/u_y(z/D = 0) \sim 1/4$. These results explain why the flow parcels at $z/D = 0$ are advected upstream more quickly than the flow parcels in close proximity to the vortical structures themselves.

Let us extend the analysis above to the cases 2W and 4W. The visual inspection of the velocity and vorticity fields (see Figs. 4 and 5) reveals that the advection of low-momentum

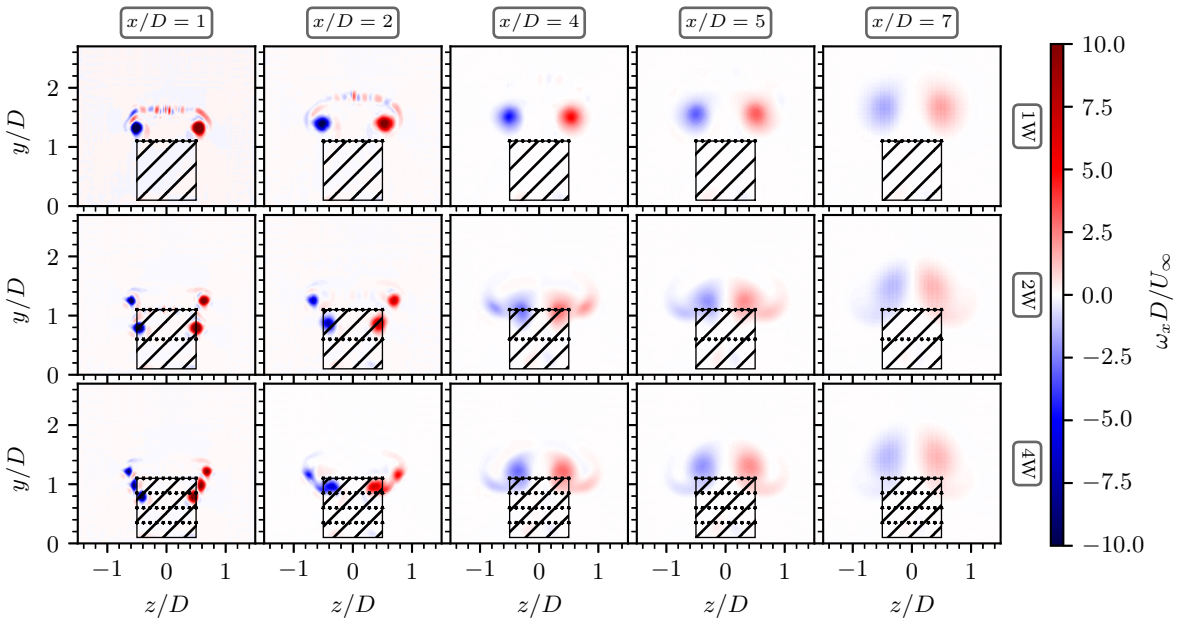

Figure 5. Streamwise-vorticity contours reveal the wing-tip vortexes generated by the different ABL-controlling device designs. Rotor's projected area is represented as a hashed region. Top-to-bottom rows show results for 1, 2, and 4 ABL-controlling wings (represented as $\star$ symbols), respectively.

fluid parcels is more efficient for setups with more wings. However, the upward advection of wing vortices is relatively slower in setups with more wings than in the setup with a single ABL-controlling wing. For cases 2W and 4W, the process of moving the wake can be seen as three-fold. Firstly, the vortical structures created by the extra wings below induce the lateral motion of the wing-tip vortices above (notice the lateral expansion of the wake in panels $x/D = 1$ in Fig. 5). Secondly, as the bottom-most vortices approximate each other in the interior region of the wake at $x/D \sim 2$, the vertical velocity one projects on another increases in magnitude, and they are quickly propelled upwards while pushing the vortices above out and downwards (see panels for $x/D = 4$). Lastly, as the vortex-coalescence forms two counter-rotating vortexes, the induction fields of these large vortexes become favorable to the upward advection of the vortices. This last step occurs approximately at $x/D = 7$ in Fig. 5. Therefore, only at $x/D \approx 7$ do the low-momentum fluid parcels swirling in the coalescence vortexes find favorable conditions to move to the higher regions of the ABL.

3.3. Momentum entrainment

In the previous subsection, the topology of the wakes of the ABL-controlled systems was assessed using velocity and vorticity fields. This subsection focuses on the momentum and energy balances of the ABL-controlled flows for the different design strategies of cases 1W, 2W, and 4W.

In Fig. 6, velocity products at a horizontal plane at $y/D = 1.1$ are used to assess the ABL-controlling effects on the vertical momentum flux qualitatively and its impact on power extraction. It's important to note that negative values of the product $-u_y u_x$ indicate momentum transfer from the flow below to the flow above the plane, while positive values indicate transfer from above to the flow below the plane. The results shown in Fig. 6 align with observations from the previous subsection. All ABL-controlled setups show a noticeable increase in vertical momentum exchange between the ABL and the wake. The $-u_y u_x$ fields also reveal a significant

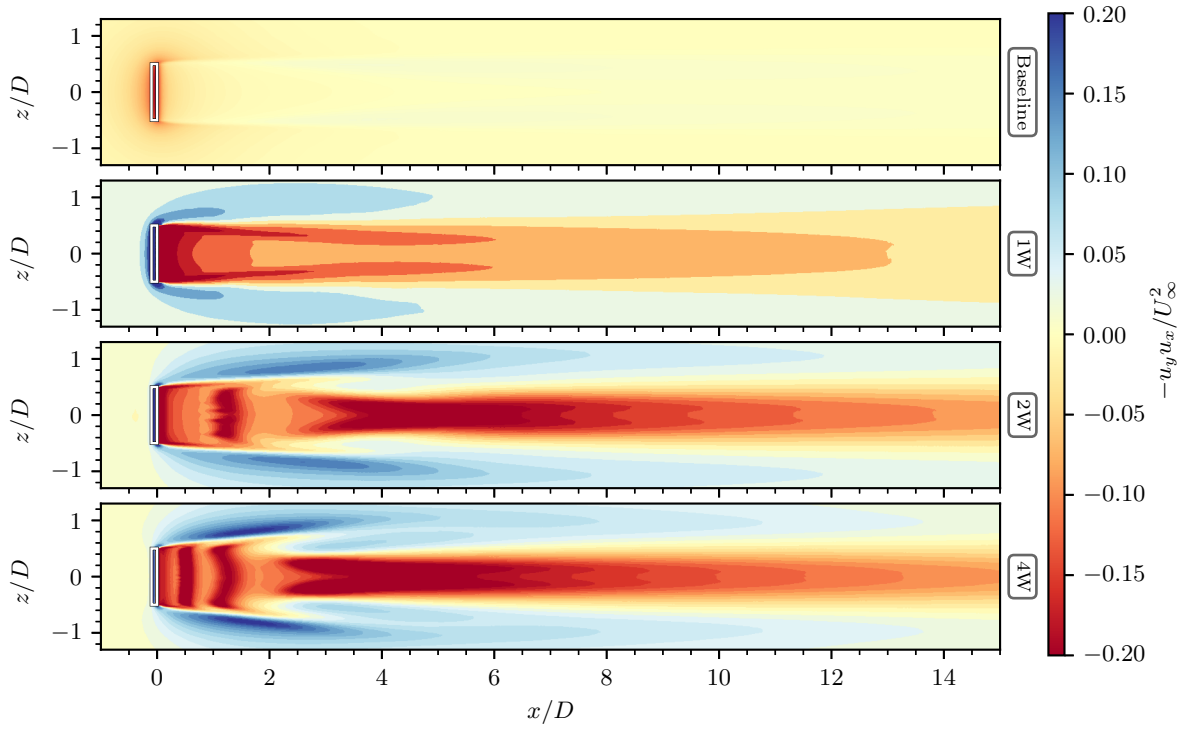

Figure 6. Products of vertical and streamwise velocities at the top of the disk actuator model plane, $y/D = 1$. Rotor's projected area is represented as black-and-white line segments.

performance improvement when the 2- or 4-wing design is adopted compared to the 1-wing design of case 1W. This improvement is attributed to the homogeneous distribution of the circulation Γ_x across the wake, effectively reducing the distance r between the wing-tip vortex's rotation center and the low-momentum flow parcels of the wake, resulting in more substantial vertical momentum fluxes across the wake.

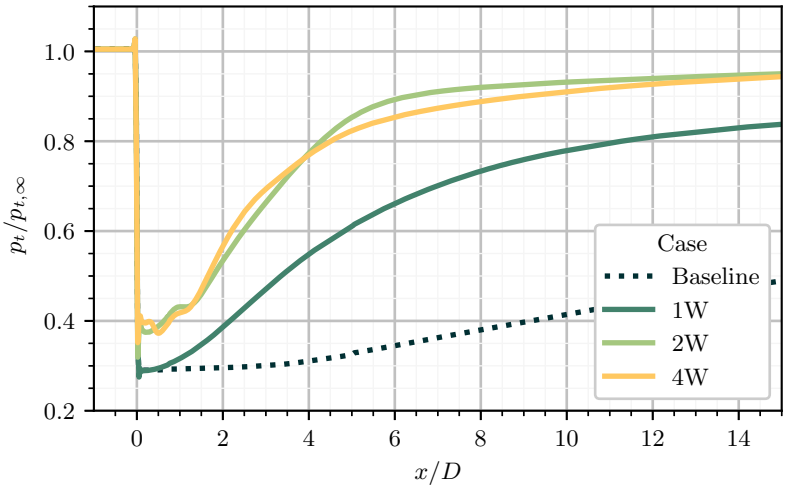

Figure 7. Total pressure available in the wake. The total pressure is integrated into a box-shaped volume of the rotor's projected area in the downwind direction.

Lastly, the efficiency of the current ABL-controlling strategy is assessed through the total pressure, p_t, available in the wake. The total pressure is integrated inside a flow volume defined by the projected cross-sectional area of the multirotor system, i.e., $x \in [0, +\infty]; y \in [0.1D, 1.1D]; z \in [-0.5D, 0.5D]$. The results are shown in Fig. 7. According to the Momentum Theory, the total pressure behind an actuator disk is $p_\infty + 1/2\rho((1-2a)U_\infty)^2$, where a is the induction in the one-dimensional streamtube idealization. The Momentum Theory also establishes that a relates to the actuator disk's thrust coefficient C_T by $C_T = 4(1-a)$. Thus, for the present system, the Momentum Theory predicts a constant value of $p_t/p_{t,\infty}(x/D > 0) \approx 0.28$. However, the current viscous wake model can recover momentum via the velocity fluctuations around the streamtube (see dotted curve). Nonetheless, it is evident that when the ABL-controlling strategy is applied, the wake recovery is considerably faster, and the velocity fluctuations become the secondary mechanism of momentum entrainment and wake recovery. In agreement with the results shown in Fig. 6, the design strategies with more wings proved more efficient in recovering the wake. For instance, in the cases 2W or 4W, the total pressure in the wake reaches 95% of the free-stream value at $x/D \approx 5$ and 6, respectively. For the baseline case without ABL-controlling devices, the same level of wake recovery is at least one order of magnitude slower, such that it could not be captured in the current computational domain.

4. Conclusions

The current study introduces and evaluates an innovative multirotor wind farm concept featuring ABL-controlling wings strategically positioned in the near wake region. These wings generate vortical structures, enhancing the vertical momentum flux from the flow above into the wind farm flow, thereby accelerating wake recovery. Employing three-dimensional actuator surface models based on Momentum Theory for multirotor and ABL-control devices, the velocity and vorticity field analyses demonstrate the crucial role of large wing-tip vortices in upwardly advecting low-momentum fluid parcels from the wake to the flow in exchange for moving downward high-momentum flow from the ABL into the wind farm flow. Momentum flux and total pressure analyses reveal that, with ABL-controlling strategies, vertical momentum flux becomes the primary driver of wake recovery, overshadowing the secondary role of velocity fluctuations under the investigated flow conditions. Notably, the two- and four-wing ABL-controlling strategies achieve 95% wake recovery at $x/D \approx 5$, showcasing promising design potential.

Acknowledgments

The authors would like to express their sincere gratitude to Thomas Broertjes for providing them with the Computer-Aided Design (CAD) model of the multirotor system.

References

[1] Abkar M and Porté-Agel F 2013 *Energies* **6**(5) 2338–2361 ISSN 19961073
[2] Ferreira C S 2009
[3] Howland M F, Lele S K and Dabiri J O 2019 *Proceedings of the National Academy of Sciences of the United States of America* **116**(29) 14495–14500 ISSN 10916490
[4] Huang M, Sciacchitano A and Ferreira C 2023 Experimental and numerical study of the wake deflections of scaled vertical axis wind turbine models *Journal of Physics: Conference Series* vol 2505 (IOP Publishing) p 012019
[5] Menter F R, Kuntz M and Langtry R 2003 *Turbulence, heat and mass transfer* **4**(1) 625–632 URL `http://aaac.larc.nasa.gov/tsab/cfdlarc/aiaa-dpw/`
[6] Hornshøj-Møller S D, Nielsen P D, Forooghi P and Abkar M 2021 *Renewable Energy* **164** 1550–1558 ISSN 18790682
[7] 1998 *Computers in physics* **12**(6) 620–631
[8] Selvam R P 2022 *Computational fluid dynamics for wind engineering* (John Wiley & Sons)
[9] Parekh J and Verstappen R W 2023 *Computers and Fluids* **257** ISSN 00457930
[10] Rezaeiha A, Kalkman I and Blocken B 2017 *Renewable Energy* **107** 373–385 ISSN 18790682